Geometrical Deep Learning: A Feasible Methodology For Predicting Age

Santiago Isaac Flores-Alonso [1], Blanca Tovar-Corona[2], René Luna-García[1]

[1] IPN,CIC, Ciudad de México 07738,
México

[2] IPN,UPIITA, Ciudad de México 07340,
México

sfloresa2010@alumno.ipn.mx, bltovar@ipn.mx, rlunag@ipn.mx

Abstract. This paper presents...

Keywords. Aging, cortical features, connectomics, GCN, PSD, ,

1 Introduction

The human brain undergoes dynamic changes throughout life, with the aging process in adulthood leading to structural and functional changes, contributing to a gradual cognitive decline [71]. Although these age-related changes are not inherently pathological, the likelihood of developing neurodegenerative disorders increases with age [2, 56]. Emerging research suggests that certain neurodegenerative conditions may stem from processes associated with accelerated brain aging [37].

In this context, preventive medicine stands to benefit from individualized quantification of atypical aging, as a significant deviation between predicted and chronological age, may indicate pathological aging [47].

Understanding and identifying biomarkers that define healthy aging is crucial to detect early-stage neurodegeneration and predicting age-related cognitive decline. One promising approach involves leveraging neuroimaging and electrophysiological data to capture the multivariate patterns of age-related brain change and formulate high-dimensional regression boundaries to accurately predict the age of healthy individuals. Machine learning (ML) models, trained on neurotypical subjects, can then be applied to clinical samples, revealing aberrant age-related changes, and offering a population-level tool for assessing brain aging. This approach has been employed in various disorders, such as Alzheimer's[24, 27, 31, 26], traumatic brain injury[11], schizophrenia [43, 75], HIV [45, 12] , epilepsy [59], and Down's syndrome[10]. Additionally, predicting brain age has extended beyond neurological disorders, showing positive impacts of meditation[51], diet [58], increased education and physical exercise [63, 68] on brain age.

The aforementioned studies have predominantly focused on estimating brain age by analyzing gray matter morphometry or spectral features from various brain regions of interest (ROIs). However, it's crucial to recognize that the brain operates as a complex network of interconnected neural circuits, facilitated by white matter tracts that directly link different brain regions [3], and functionaly supported by the coordinated activity between these distinct, separated brain regions [61]. Both structural and functional connectivity within this neural network undergo significant age-related

changes during healthy aging [15], and exhibit distinct patterns in various neuropathologies [54, 48, 50]. Surprisingly, these properties have often been overlooked as potential features for predicting brain age.

To explore the significance of brain topology and in the pursuit of integrate it with functional and structural information into age prediction models, we employed a Graph Convolutional Networks (GCN) architecture on graphs generated from resting-state MEG data and structural connectivity measures derived from diffusion MRI. Within this framework, each node was annotated with both gray matter morphometry and spectral features.

2 Related Work

Numerous studies have delved into the intricate dynamics of age-related changes in the human brain, recognizing the crucial role of these alterations in cognitive decline and the onset of neurodegenerative disorders. These investigations underscore the potential of individualized quantification of atypical aging as a means for the early detection of pathological conditions.

In this section, our focus shifts exclusively to works published between 2018 and 2023 that leverage the identical dataset detailed in Section 3.1, either independently or in conjunction with another database. As depicted in Table 1, the aforementioned studies predominantly concentrate on estimating brain age based on morphometric or spectral data from different brain regions of interest (ROIs), extracted from structural magnetic resonance imaging (T1-weighted MRI) [cite] and M/EEG data, with the former being the most prevalent and exhibiting the best performance. However, most overlook the underlying topology of the brain, neglecting critical information related to the neighborhood, connectivity, or distribution of power and frequencies among ROIs.

A couple of works have explored topological features using 3D Convolutional Neural Networks (3D CNN), capturing the spatial distribution of gray and white matter in T1-weighted MRI images. Additionally, 2D CNNs have been employed to capture the spatial topology of connectomes [49]. Nevertheless, CNNs, designed for Euclidean spaces, may yield misleading conclusions when applied to graphs, given their inherent non-Euclidean structure. Furthermore, CNNs cannot incorporate node embeddings in the graph as part of the feature space.

It is essential to note that a variety of feature extraction techniques have been employed, with both linear and nonlinear approaches, demonstrating comparable performance. While these studies validate the effectiveness of their chosen techniques, none has dedicated itself to methodologies that integrate electrophysiological, morphological, and connectomical data into a framework that best aligns with the brain's architecture. In contrast, the present work achieves this integration through the use of Graph Convolutional Networks (GCN).

3 Materials and Methods

This section encapsulates the feature extraction techniques and Deep Learning algorithm employed to tackle the challenge of age prediction, accompanied by a detailed description of the dataset. The proposed algorithm was implemented in Python 3.9 on the Ubuntu 20.04 distribution. Specifically, the deep learning model was constructed utilizing PyTorch version 2.0.1.

3.1 Dataset

We conducted the analysis using data sourced from the open-access Cambridge Center for Aging Neuroscience (Cam-CAN) repository (refer to [62, 65], for detailed information on the dataset and acquisition protocols). The dataset is accessible at http://www.mrc-cbu.cam.ac.uk/datasets/camcan/.

Specifically, our investigation utilized neuroimaging and electrophysiological data from a cohort of 652 healthy subjects (male/female = 322/330, mean age = 54.3 ± 18.6, age range 18–88 years). After exclusions, which involved subjects lacking both MRI and MEG data, unsatisfactory

Table 1. Comparative table between works that used the same dataset

Title	Dataset	Year	Technique	N	Features	ML \ AI Technique	Performance
An augmented aging process in brain white matter in HIV [44]	Healthy: CamCAN ; UIO, HIV: UCLA	2018	DTI-MRI	765	Parcellation: Selected ROIs from a non conventional parcellation, Global graph metrics from structural connectivity	SVR	Healthy: R=.84, R²=.7, MAE=7.39. HIV: R=0.64, R²=0.41, MAE=9.48.
Bayesian Optimization for Neuroimaging Pre-processing in Brain Age Classification and Prediction [44]	CamCAN	2018	T1-MRI	648	T1 gray matter volume images were vectorized (ASCII-format intensity values) and used as features.	SVM-R	Classification: Old(>55) vs Young(16-22). Acc = 88.1. Regression: R = 0.91, R²= 0.83, MAE = 5.46 years.
Estimating brain age based on a uniform healthy population with deep learning and structural magnetic resonance imaging [22]	14 open datasets including CamCAN	2020	T1-MRI	10157	Full resolution 3D T1w MRI images	3D deep convolutional neural network	Full dataset: R=0.97, MAE=4.06, CamCAN: MAE = 6.08, R=.929.
Interpretable brain age prediction using linear variable models of functional connectivity [54]	CamCAN, HCP, ATR	2020	fMRI	?	Parcellation: 264, 10 mm regions. Amplitude Correlation (Pearson's) for functional connectivity. Linear latent variable model: PCA, Non neg. PCA, Modular Hierarchical analysis (MHA), Modular Connectivity Factorization (MCF), ICA	Linear Regression	MAE 9.5
Functional brain age prediction suggests accelerated aging in preclinical familial Alzheimer's disease [31]	7 open datasets including CamCAN	2020	fMRI	1340	Parcellation: 272 regions corresponding to the Power and Petersen functional atlas. Amplitude Correlation (Pearson's) for functional connectivity.+ Fisher's Z-transformed. 26 Global graph features.	SVR	Healthy: R=.72, R²=.53, MAE = 11.00 AHD: R=.6, R²=.36, MAE= 11.58
Generalization of diffusion magnetic resonance imaging-based brain age prediction model through transfer learning [6]	CamCAN, National Taiwan University Hospital (NTUH), Hammersmith Hospital (HH), Guy's Hospital (Guys)	2020	DTI-MRI	1380	Features of white matter tract integrity for machine learning, tract-based automatic analysis was performed to sample the diffusion indices from 76 predefined major fiber tract bundles over the whole brain. Description at 10.1002/hbm.22854	6 layer Cascade NN	R = .94, MAE = 4.68
Chapter on International Workshop on Predictive Intelligence In Medicine: Improving Across Dataset Brain Age Predictions Using Transfer Learning	7 open datasets including CamCAN	2021	T1-MRI	2543	Trained on full resolution 3D T1w MRI images	CNN + Transfer learning	MAE = 3.70
Association vs. Prediction: The Impact of Cortical Surface Smoothing and Parcellation on Brain Age [72]	CamCAN	2021	T1-MRI	608	Parcellation: 100,200,400,1000 Shaefer. Cortical thickness + PCA	Linear Regression	R = .63, R²=.4, RMSE =9.5
Learning patterns of the ageing brain in MRI using deep convolutional networks [30]	UK Biobank	2021	T1-MRI	12,802	Reshape to 128x128x20 3D T1w MRI images	3D CNN	R = .889, R²=.77, MAE = 3.9
A reusable benchmark of brain-age prediction from M/EEG resting-state signals [21]	CamCAN(MEG), LEMON(EEG), CHBP(EEG), TUAB(EEG).	2022	MEG/ EEG	2540	Parcellation: 448. Statistical properties of the PSD, spectral features as CWT, information theory of the time series (entropy, fractality), Filterbank (computes covariances from several narrow-band signals) based on Riemannian geometry	Time series: ShallowFBCSPNet, Deep4Net. Features:Ridge Regression, RF	R=.86, R²=.74, MAE=7.3
Brain Age Prediction with 3D ResNet34 Model in Healthy Control, Mild Cognitive Impairment, and Alzheimer's Disease [38]	CamCAN (Healthy) and ADNI (Mild Cognitive Impairment and Alzheimer)	2022	T1-MRI	764	Reshape to 256x256x256 3D T1w MRI images	3d resnet34	MAE = 18
Ayu-Characterization of healthy aging from neuroimaging data with deep learning and rsfMRI [5]	CamCAN	2022	fMRI	172(20-40 yo), 152(41-51 yo), 154 (56-69 yo), 160(70-88 yo) = 638	Parcellation: Shaefer 100. Amplitude Correlation (Pearson's) for functional connectivity.	AlexNet, VGGNet5, and ResNet5	Classification: Acc = .726 Regression : MAE = .6.7, R=.86, R²=.754
Mind the gap : Performance metric evaluation in brain-age prediction [16]	CamCAN / UK Biobank	2022	T1-MRI	41,907	Parcellation: 68 Desikan Killany. Morphometric features: Volume, surface area, mean and std. Cortical thickness, mean curvature, gaussian curvature, folding index, intrinsic curvature.	XGBoost regression algorithm	R = .889, R²=.790, MAE= 6.79
Regional Neuroanatomic Effects on Brain Age Inferred [53]	ADNI, HCP, UK Biobank, CamCAN	2022	T1-MRI	4069	Parcellation: 148, Morphometric features: Volume, surface area, mean thickness, mean curvature	Ridge Regression	Non Corrected: R=.9, R²=.82, MAE = 6.66 Corrected= R=1, R² = 1, MAE=0.08
Brain-age prediction: A systematic comparison of machine learning workflows [55]	CamCAN, IXI, eNKI, 1000Brains	2023	T1-MRI	2953	In the first strategy, voxel-wise GMV (Grey matter volume) after smoothing and resampling + PCA. In the second strategy, an atlas to summarize data from distinct brain regions	Ridge Regression, lasso, elastic net, kernel ridge regression, random forest, Gaussian Process Regression (GPR), Relevance Vector Regression (RVR)	R=.94, R²=.89, MAE = 4.94.
Brain age prediction using combined deep convolutional neural network and multi-layer perceptron algorithms [41]	1000FCP, INDI, IXI, OASIS-3, OpenNeuro, CamCAN	2023	T1-MRI	3004	For 3D CNN : Reshape to 105x127x105 3D T1w MR images. For MLP: "Categorical Sex information".	3D CNN, MLP	R=.96, R² = .93, MAE = 3.49
The Choice of Machine Learning Algorithms Impacts the Association between Brain-Predicted Age Difference and Cognitive Function [47]	CamCAN	2023	T1-MRI	601	Parcellation: 68 Desikan-Killary. Morphometric features: Volume, mean cortical thickness, surface area and 16 measures of subcortical structures.	Linear Regression, Ridge, Lasso, Elastic Net, SVR, Relevance Vector Regression (RVR), Gaussian Process Regression (GPR)	R=.91, R² = .82, MAE= 5.93
Brain Structure Ages - A new biomarker for multi-disease classification [56]	17 open datasets including CamCAN	2023	T1-MRI	32718	Parcellation: 133. Preprocessing and reshaping to 91 × 109 × 91, extract 3 overlapping sub-volumes of the same size 32 × 48 × 32 voxels and evenly distributed from the downscale image. U-Nets to predict age at voxel level with these "m" sub-volumes. The "m" outputs were then used to reconstruct a 3D map of size 91 × 109 × 91 voxels. Age correction technique for each voxel. Average over parcellations.	U-net, MLP, SVM.	For young: R=.95, R²=.91.MAE = 1.91, For Old: R=.78, R²=.61, MAE = 3.87. They use 100% of the data. This are the training results.
A Siamese Network With Node Convolution for Individualized Predictions Based on Connectivity Maps Extracted From Resting-State fMRI Data [70]	CamCAN	2023	fMRI	568	Parcellation: 200, Amplitude Correlation (Pearson's) for functional connectivity	Siamese network with node convolution (SNNC)	R = .9, R²=.81, MAE = 6.2
From Signal to Age – Using machine learning to predict brain age from MEG data [39]	SBDL (Salzburg Dynamic Brain Lab), CamCAN	2023	MEG	1625	Sensor Level. Statistical features from the time series	Random Forest	R = .62, R²=.38
A Multitask Deep Learning Model for Voxel-Level Brain Age Estimation [29]	CamCAN, Calgary Campinas Study Dataset	2023	T1-MRI	651	T1 Preprocessing and reshape to 128x128x128	U-Net	MAE = 5.30 ± 3.29
Brain Age Revisited: Investigating the State vs. Trait Hypotheses of EEG-derived Brain-Age Dynamics with Deep Learning [28]	RNP, RP, TNPP, and TPNP	2023	EEG	6035	Windowing of times series form 21 channels. 15 min recordings	temporal convolutional network (TCN)	MAE = 6.6
Prediction of individual brain age using movie and resting-state fMRI [4]	CamCAN	2023	FMRI + MRI movie	656 + 256	Parcellation: 264. Amplitude Correlation (Pearson's) for functional connectivity	Elastic Net Regression	R = .86, MAE=7.3

preprocessing results or failure to extract the cortical surface for source reconstruction, our final dataset comprised 606 subjects.

3.1.1 Magnetic Resonance Imaging

All Magnetic Resonance Imaging (MRI) datasets were collected at a single site (MRC-CBSU) using a 3T Siemens TIM Trio scanner with a 32-channel head coil.For the T1-weighted MRI the imaging parameters of the MPRAGE sequence were: TR = 2250 ms, TE = 2.99 ms, Flip angle = 9°, Field of View = 256 × 240 × 192 mm³, and voxel size = 1 mm isotropic.

For the multi-shell diffusion-weighted MRI (dMRI) (b=0,1000,2000), the imaging parameters of the Twice-refocused SE sequence were: TR = 9100 ms, TE = 104 ms, Field of View = 192 × 192 mm² , and voxel size = 2 mm isotropic.

3.1.2 Magnetoencephalography

Resting-state magnetoencephalography (MEG) data were captured utilizing a 306-channel Elekta Neuromag Vectorview system, comprising 102 magnetometers and 204 planar gradiometers. The recordings took place in a well-lit magnetically shielded room, with a sampling rate of 1 kHz and a highpass filter set at 0.03 Hz. Throughout the resting-state scan, participants were instructed to maintain stillness, stay awake, and keep their eyes closed for approximately 9 minutes. Continuous estimation of head position within the MEG helmet was conducted using four Head-Position Indicator (HPI) coils, enabling offline correction of any head movement. Additionally, two pairs of bipolar electrodes were employed to capture vertical and horizontal electrooculogram (VEOG, HEOG) signals, facilitating the monitoring of blinks and eye movements. Furthermore, one pair of bipolar electrodes recorded the electrocardiogram (ECG) signal to monitor pulse-related artifacts.

3.2 MEG data preprocessing and feature extraction

MEG preprocessing procedures closely followed the methodology outlined in [13], adhering to established good-practice guidelines [32]. Data analysis was performed with Brainstorm[64] in MATLAB 2020b (Mathworks, Inc., Massachusetts, USA), which is documented and freely available for download online under the GNU general public license (http://neuroimage.usc.edu/brainstorm).

Firstly, a notch filter bank was applied to eliminate the line noise artifact (60 Hz) and 3 of its harmonics. Slow-wave and DC-offset artifacts were then removed using a highpass FIR filter with a 0.3-Hz cutoff. Signal-Space Projections (SSPs) [67] were derived to effectively remove cardiac and ocular artifacts. This involved defining signal projectors based on electrocardiogram and electroculogram recordings around identified artifact occurrences. SSPs were also applied to attenuate low-frequency (1–7 Hz) and high-frequency noisy components (40–400 Hz) related to saccades and muscle activity, respectively.

Subsequently, distinct brain source models were generated for all narrowband versions of the MEG sensor data. Individual T1-weighted MRI data were automatically segmented and labeled with Freesurfer [14]. Co-registration with MEG sensor locations was established using digitized head points collected during each MEG session. MEG forward head models were created for each participant using the overlapping spheres approach [36], and cortical source models were developed with linearly constrained minimum-variance (LCMV) beamforming [74]. Data covariance regularization was performed, and to mitigate the impact of variable source depth, the estimated source variance was normalized by the noise covariance matrix. Elementary MEG source orientations were constrained normal to the surface at 15,000 locations of the cortex. Noise statistics for source modeling were estimated from two-minute empty-room recordings collected as closely as possible in time to each participant's MEG session.

Finally, the source time series were organized into 68 and 200 cortical regions of interest (ROIs) based on the Desikan-Killiany(DK) and Schaefer-200 (s200) atlases, respectively, which constitute the nodes of the graphs. To streamline the time series within each ROI, dimension reduction was performed using the first principal component computed using principal component analysis (PCA) [69]. To standardize the intersubject variability duration in the recordings, the time series were uniformly cropped to a duration of 300 seconds.

3.2.1 Power Spectrum Density

After estimating the mean time series for each region of interest (ROI), spectral power density (PSD) was computed using the Welch method, involving: (1) Dividing the original data segment into K possibly overlapping segments; (2) Calculating the periodogram by computing the Discrete Fourier Transform (DFT) for each segment, then squaring the magnitude and dividing by the length; (3) Averaging these local estimates.

Formally, the estimation method is as follows. For each segment of length L, a modified periodogram is computed by selecting a data window $W(j), j = 0, \ldots, L - 1$, and forming the sequences $X_1(j)W(j), \ldots, X_K(j)W(j)$. The finite Fourier transforms $A_1(n), \ldots, A_K(n)$ of these sequences are then obtained:

$$A_k(n) = \frac{1}{L} \sum_{j=0}^{L-1} X_k(j)W(j)e^{-i\frac{2kj}{L}} \quad (1)$$

The K modified periodograms are given by:

$$I_k(f_n) = \frac{L}{U}|A_k(n)|^2, \quad k = 1, 2, \ldots, K, \quad (2)$$

where

$$f_n = \frac{n}{L}, \quad n = 0, \ldots, L/2$$

and

$$U = \frac{1}{L} \sum_{j=0}^{L-1} W^2(j).$$

Finally, the spectral estimate is the average of these periodograms, i.e.,

$$\hat{P}(f_n) = \frac{1}{K} \sum_{k=1}^{K} I - k(f_n). \quad (3)$$

To capture the ROI-wise spectral features, a two-second window with a 50% overlap was employed for computing the PSD, effectively encoding the frequencies between 0 and 500 Hz with a 0.5 Hz resolution. In Figure 1.A, the mean global PSD (averaging across all ROIs) is depicted averaged across subjects over 5-year intervals. Particular emphasis is placed on frequencies ranging from 5 to 35 Hz (alpha and beta bands), as this range prominently showcases age-related changes in power distribution.
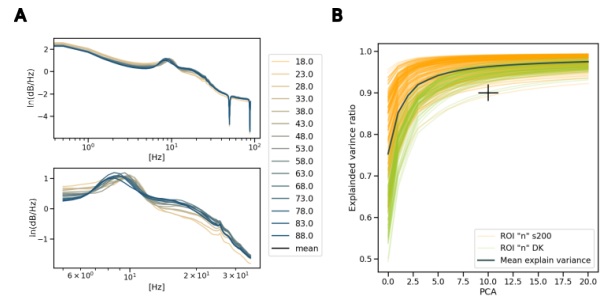

Fig. 1. A. Mean Global PSD: The global PSD was computed by averaging the PSD within each parcellated brain region. The mean global PSD represents the average across all subjects, grouped in intervals of 5 years. B. PCA per ROI. Each curve represents the explained variance for each ROI within the DK, s200 atlases, as function of the number of principal components. The solid black curve is the mean explained variance.

Given the disparity between the participant count and the number of spectral features (ROIs x PSD), there is a risk of data sparsity, complicating the model's ability to discern meaningful patterns. Hence, PCA was chosen as the dimensional reduction technique. Figure 1.B illustrates the

explained variance for the first 20 components for each ROI within each atlas. As the cross indicates, the first 10 components are sufficient to explain at least 90% of the variance for all ROIs, resulting in a 99% reduction in the volume of the searching space.

3.2.2 Functional Connectivity

Functional connectivity entails examining the statistical relationships and temporal dependencies among distinct brain regions or neuronal populations [23]. Employed in neuroimaging, it gauges the extent to which the activities in various brain areas correlate or synchronize over time.

The observed co-activation patterns between brain regions serve as indicators of the brain's functional network organization [72]. High synchronization implies the participation of spatially separated regions of interest (ROIs) in similar neural processes, while low connectivity suggests diminished coordination among these regions. Aberrant connectivity may indicate the presence of diverse neurological and psychiatric conditions. To calculate the degree of synchronization, the amplitude envelope correlation (AEC) [6] was employed.

As it's name implies, the AEC uses the amplitude envelopes to derive the corresponding Pearson correlation coefficients between all pair of ROIs. Firstly, the Hilbert transform [9] was employed to decompose time series into the time-frequency domain for envelope computation. The Hilbert transform $\mathcal{H}[x(t)]$ of a signal $x(t)$ is expressed as:

$$\mathcal{H}[x(t)] = \frac{1}{\pi} \int_{-\infty}^{\infty} \frac{x(t-\tau)}{\tau} d\tau = a_{\tilde{x}}(t)e^{j\phi_{\tilde{x}}(t)} \quad (4)$$

$$\mathcal{H}[x(t)] = \frac{1}{\pi} \int_{-\infty}^{\infty} \frac{x(t-\tau)}{\tau} d\tau = a_{\tilde{x}}(t)e^{j\phi_{\tilde{x}}(t)} \quad (5)$$

The result, often denoted as $\tilde{x}(t)$, is an analytic signal—a complex time series uniquely associated with the original data time series, $x(t)$, where the modulus $a_{\tilde{x}}(t)$ and phase $\phi_{\tilde{x}}(t)$ of $\tilde{x}(t)$ correspond to the instantaneous amplitude (or envelope) and instantaneous phase of the original time series $x(t)$, respectively.

However, in the process of deriving power envelopes for correlation analysis, a crucial step involves orthogonalizing the two signals that may be correlated [34]. This ensures that the signals do not share trivial co-variability in power, arising from measuring the same sources, while preserving co-variation related to measuring different sources.

By employing ordinary least squares, the instantaneous linear relation between two signals in the frequency domain can be derived. Let $X(t, f)$ and $Y(t, f)$ represent the frequency domain representations of two time series x and y, where t and t' are the time points of the center of the windows for spectral analysis, and f is the frequency of interest. The part of a complex time series Y that can be instantaneously and linearly predicted from X, denoted as $Y_{\|X}$, is expressed as:

$$Y_{\|X} = real(\frac{\sum_{t' \in T} X(t', f)Y(t', f)^*}{\sum_{t' \in T} X(t', f)X(t', f)^*})X(t, f) \quad (6)$$

Where $a_{X,Y}$ is the regression coefficient describing the instantaneous linear relation between X and Y, estimated from data in the time interval T, $*$ denotes the complex conjugate, and real($\cdot$) is the real part of a complex number. The signal Y orthogonalized to the signal X, denoted as $Y_{\perp X}(t, f)$, is derived by subtracting the parallel signal component:

$$Y_{\perp X}(t, f) = Y(t, f) - Y_{\|X}(t, f) \quad (7)$$

The orthogonalized AEC where used to compute the individual connectomes derived for each one of the typical frequency bands of electrophysiology to understand whether the expression of certain ranges of brain rhythms would explain better the age differentiation as shown if Figure 2. We bandpass filtered MEG signals in the delta (1–4 Hz), theta (4–8 Hz), alpha (8–13 Hz), beta (13–30 Hz), gamma (30–50 Hz), and high gamma (50–150 Hz) frequency bands.
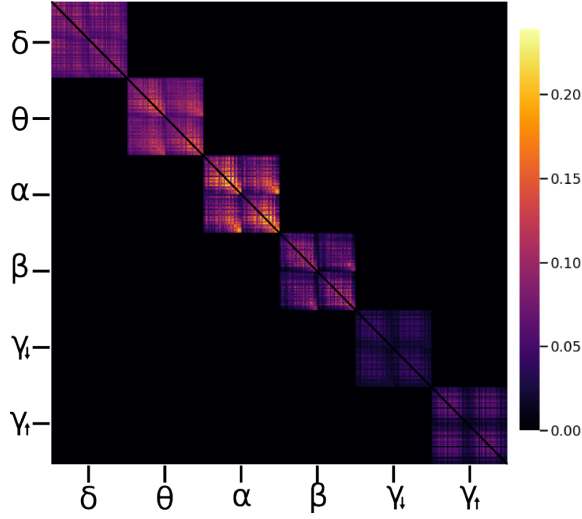
Fig. 2. Functional connectivity: The connectomes where computed using the orthogonalized AEC for each one of the six canonical bands (delta, theta, alpha, beta, low-gamma and high-gamma). This heatmap, build using diagonalizing the mean connectomes for each band, is only for visualization purposes. Each one of the connectomes where used individually.

Given that the AEC returns the pairwise correlation value, the resulting connectome is a fully connected graph containing non-relevant connections, with low correlation values. To generate a sparse graph, the connectomes were thresholded using Kruskal's Minimum Spanning Tree (MST) algorithm [44]. Finally the diagonal of the each one of the connectomes (autocorrelation) were set to zero.

The calculation of the Pearson correlation for all pairwise regions has a computational complexity of O^2. This, added to the fact that we will use six different narrowband frequencies for 606 subjects, led us to compute the connectome using only the DK atlas. Therefore, each one of these connectomes, yields a 68 × 68 symmetric connectome matrix.

The correlation

3.3 Gray Matter Morphometry and Structural Connectivity

The preprocessing of the raw NIfTI data in Brain Imaging Data Structure (BIDS) format from the CamCAN repository were executed utilizing the official singularity container images. The adoption of singularity container images was pivotal in ensuring the reproducibility of the entire preprocessing process. This rigorous approach adheres to established standards and safeguards the integrity and consistency of the data processing workflows.

3.3.1 Gray Matter Morphometry

Magnetic resonance imaging (MRI) is a technique used in medical imaging that generates images that provide contrast between different tissues, taking advantage of the magnetic moment and spin of hydrogen protons present in the tissue.

Hydrogen has a non-zero net spin and can be affected by an external magnetic field $B_{0_{\hat{z}}}$. In the presence of $B_{0_{\hat{z}}}$, the protons will align and precede around the axis defined by the magnetic field with a frequency defined by

$$\omega = \gamma B_{0_{\hat{z}}} \tag{8}$$

as described by the Larmor equation where, γ is the gyromagnetic constant. The sum of the magnetic moments of the proton i, within a volume V (voxel), will define the local magnetic moment, or magnetization vector, as

$$\vec{M} = \frac{1}{V} \sum_i \vec{\mu}_i \tag{9}$$

where V must be small enough for $B_{0_{\hat{z}}}$ to be constant, but large enough to contain a sufficient number of protons.

If the interactions of the protons with their surroundings are ignored, the sum of the equations of motion for individual spins gives

$$\frac{1}{V} \sum_i \frac{d\vec{\mu}_i}{dt} = \frac{\gamma}{V} \sum_i \mu_i \times B_{0_{\hat{z}}} \tag{10}$$

which can be rewritten as

$$\frac{d\vec{M}}{dt} = \gamma \vec{M} \times B_{0_{\hat{z}}} \tag{11}$$

If only the B0 field exists, this longitudinal magnetization will be in equilibrium and will be called $M0$.

However, if a second pulse $B1$ is applied, perpendicular to B0, in resonance with the precession frequency, the magnetization vector will move away from z, towards the transverse plane, with an angle defined by:

where tau is the exposure time to B1. Once pulse B1 is removed and as a result of the continued presence of the static field, the magnetization returns to its equilibrium magnetization vector M0zˆ. The relaxation of the magnetization vector from the transverse to the longitudinal plane is dependent on the interactions of the spins with the medium, where the moment will tend to align parallel to the field to reach its minimum energy state, as long as the energy can be transferred.

The preprocessing of anatomical MRI data was conducted utilizing fMRIPrep version 23.0.1, as outlined by Esteban et al. (2019). fMRIPrep is a tool specialized in preprocessing magnetic resonance imaging (MRI) data, that incorporates a series of steps for the thorough processing of T1-weighted (T1w) anatomical images. In a nutshell, the preprocessing involves addressing intensity nonuniformities (INU) in the T1w images to ensure consistency, removal of non-brain tissues achieved through the process of skull-stripping, tissue segmentation to delineate different anatomical structures and surface reconstruction for detailed cortical and subcortical analyses. Finally, a spatial normalization aligns T1w images to a standard space, facilitating cross-subject comparisons. For a more detailed account of the original preprocessing steps executed by fMRIPrep, interested readers are encouraged to refer to tool's documentation, facilitating adaptability to varying experimental needs.

Post-preprocessing, fMRIPrep derives anatomical statistics for each ROI that encompass key metrics such as:

1. **Surface area**: Given the geometry of the reconstructed cortical surface as a mesh, for a triangular face ABC of the surface representation, with vertex coordinates $\mathbf{a} = [x_A; y_A; z_A]'$, $\mathbf{b} = [x_B; y_B; z_B]'$, and $\mathbf{c} = [x_C; y_C; z_C]'$, the area is $|\mathbf{u} \times \mathbf{v}|/2$, where $\mathbf{u} = \mathbf{a} - \mathbf{c}, \mathbf{v} = \mathbf{b} - \mathbf{c}$.

2. **Cortical thickness**: Cortical thickness is the distance between the pial surface (outer boundary of the cortex) and the gray/white matter boundary. It is given by:

$$T = \frac{(P_F - P_F^1) + (P_F^1 - P_F^1)}{2} \tag{12}$$

where P_F is a point in on the white surface boundary, and P_F^1 and P_F^2 are the nearest points to P_F on the pial and white boundaries respectively.

3. **Gray matter volume**: For a given face $A_w B_w C_w$ in the white surface, and its corresponding face $A_p B_p C_p$ in the pial surface, define an oblique truncated triangular pyramid. Subsequently, split this truncated pyramid into three tetrahedra, defined as:

$$
\begin{array}{ccccccc}
T_1 & = & (& A_w, & B_w, & C_w, & A_p &) \\
T_2 & = & (& A_p, & B_p, & C_p, & B_w &) \\
T_3 & = & (& A_p, & C_p, & C_w, & B_w &)
\end{array}
$$

For each such tetrahedra, let $\mathbf{a}$, $\mathbf{b}$, $\mathbf{c}$ and $\mathbf{d}$ represent its four vertices in terms of coordinates $[x \quad y \quad z]'$. Finally, compute the volume as $|\mathbf{u} \cdot (\mathbf{v} \times \mathbf{w})|/6$.

4. **Mean and Gaussian Curvature**: The extrinsic curvature is a property that arises from the mechanical folding of a surface, and as such is not intrinsic of the surface itself, but rather of how it is embedded in three-dimensional space. At each point on a line, the curvature is measured as the inverse of the radius of the osculating circle $c = \frac{1}{r}$. On a surface, among the infinity of possible directions, there are always two $(c1, c2)$ which produce maximum and a minimum value of curvature, and these directions are always orthogonal to each other, called the principals of curvatures.

The mean curvature H is the arithmetic mean of these principal curvatures: $H = \frac{c_1 + c_2}{2}$, while the Gaussian curvature is the product of the principal curvature measured in each of these directions $K = c1 \times c2$

5. **Intrinsic Curvature Index**: As its name suggests, the intrinsic curvature of the surface itself is a property that cannot be removed from it without tearing or deforming the surface. The intrinsic curvature of the vertex, as proposed by the principles of the Gauss-Bonnet, is calculated as the surfeit or deficit of the vertex angle divided by one third the sum of the vertex areas:

$$K = \frac{2\pi - \sum_i \theta_i}{\frac{1}{3} \sum_i A_i} \tag{13}$$

where θ_i is the angle subtended by ith vertex, and A_i is the area of ith vertex (the sum of areas of

triangle surrounding the vertex).

6. **Folding Index**: Aldo known as gyrification index, is a metric that quantifies the amount of cortex buried within the sulcal folds as compared with the amount of cortex on the outer visible cortex. It is commonly computed on coronal sections using the following equation:

$$GI = \frac{\sum_{j=1}^{M_P} A_P^j}{\sum_{j=1}^{M_O} A_O^j} \tag{14}$$

where A_P^j and A_O^j are the area of the face j in the 3-D mesh of the pial surface and of the outer surface, respectively, and M_P and are M_O the total number of faces in the pial and outer mesh, respectively.

7. **Number of vertices**: As the name implies, it is the number of vertices of the reconstructed cortical surface inside each ROI.

All of these features will be use as node attributes in the connectomes graph generated by the tractography, as explained in the next secction.

3.3.2 Structural Connectivity

Structural connectivity refers to the anatomical pathways and connections formed by white matter tracts in the brain, indicating the physical wiring that enables communication between different regions.

Aside from the extensive tracts linking the brain to the body, intricate neural circuits are constituted by connections between various cortical and subcortical regions. Employing computational reconstruction methods grounded in diffusion-weighted magnetic resonance imaging (dMRI), facilitates the visualization and mapping of the pathways of white matter tracts within the brain [52].

To reconstruct the structural connectivity matrices, a technique known as "Multishell-multitissue constrain spherical deconvolution" was use. In the next paragraphs, we will aim to briefly explain the concepts on which it is based, but we invite the reader to refer to the citated works for deeper explanations.

Diffusion-weighted MRI is a non-invasive technique sensitive to the microscopic motion (diffusion process) of water molecules. In biologic tissues, the diffusion process is influenced by the presence of biologic membranes and macromolecules (Walter and Hope, 1971), which can hinder and/or restrict the molecular random walk in both isotropic and anisotropic fashions, unraveling the geometry of the underlying structure.

In 1905, Einstein demonstrate that the Brownian motion of a particle in a fluid is characterized by the diffusion coefficient,

$$D = \frac{k_B T}{6\pi \mu_{sol} rA} \tag{15}$$

where k_B is the Boltzmann constant, μ is the viscosity and rA is the size of the particle. For the case of free diffusion, the probability distribution function for the motion

$$p(\mathbf{r}, \mathbf{t}) = \frac{1}{\sqrt{(4\pi t)^3 D}} exp\left(\frac{\mathbf{r}^T \mathbf{r}}{4tD}\right) \tag{16}$$

This Gaussian property remain true only in case of the boundless and free environment. Unfortunately, this is not the preserved in the human brain, which large part of it consists of bounds of parallel fibers interconnecting various functional areas of the cortex. Hence, diffusion in no longer free.

In order to measure the level of anisotropy and reconstruct the tracts, one can take advantage of the electromagnetic properties of the water molecule: By generating a strong enough magnetic field, the protons can be aligned parallel to the field precessing at

$$\omega = \gamma B \tag{17}$$

as describe by the Larmor equation where, γ is the gyromagnetic constant, and B is the strength of the static magnetic field. If one now apply a magnetic diffusion-sensitizing gradient $\mathbf{G}$ instead of a static field, the protons precess frequency will slightly differ across $\mathbf{G}$.

If, after a Δt, $-\mathbf{G}$ is applied, two things may happen: If there is little to non displacement, gradient will nullify, molecules will precess at the same frequency and the signal $\mathbf{S}$ produce by the synchronized protons will be maximum. On the other hand, if the protons have displacement due to the lack of tissue hindering the particle movement, these will experience $\mathbf{G}$ and $-\mathbf{G}$ in different spatial positions which will increase the inhomogeneities in the precessions abolishing $\mathbf{S}$.

G is not bounded to one direction, actually, to reconstruct the tracts in all possible directions, **G** can take as many directions as needed in a 3D space, forming a discrete spherical grid or shell. The strength and timing of the diffusion-sensitizing gradients applied during the imaging sequence is parametrized by the b-value defined as:

$$b = \gamma^2 |\mathbf{G}|\delta^2 \left(D\frac{\delta}{3} \right) \tag{18}$$

where $|G|$ is the intensity of the gradient and δ is the duration of the gradient pulse. It is easy to see that by modifying b, a different shell will be created. If multiple b-values are used to reconstruct **S**, then the approach will get the name of "multishell".

In practice a static repulsion algorithm [40] can be used to generate N quasi-uniformly distributed points on the sphere where the gradient directions $\mathbf{g}_i = (\theta_i, \phi_i), 1 \geq i \geq N$ define the sampling directions to generate the signal $\mathbf{S}(\mathbf{g_i})$, for each imaging voxel.

To model **S**, spherical harmonic (SH) transform can be use. The SH [57] is the equivalent of the Fourier transform in the plane but on the sphere. Spherical harmonics consist of a set of functions of order l and phase m, $Y_l^m(\theta, \phi) : S_2 \rightarrow \mathbf{C}$, where S_2 is the unit sphere in 3D, which we parametrize by $\theta \in [0, \pi)$ and $\phi \in [0, 2\pi)$, the angles of latitude and longitude, respectively; **C** is the set of complex numbers. Hence, the problem is to find the best coefficients of the modified SH basis that describe the HARDI signal **S** at each of the N diffusion-weighted gradient encoding directions $\mathbf{g}_i$.

Thus, the smooth estimation of the HARDI signal **S** can be formulated as:

$$S(\theta_i, \phi_i) = \sum_{l=0}^{\infty} \sum_{m=-l}^{l} C_l^m Y_l^m(\theta_i, \phi_i) \tag{19}$$

Due to orthonormality of the SH basis, the coefficients of the SH series C_l^m can be calculated by forming the inner product of **S** with the spherical harmonics, given by:

$$C_l^m = \langle S(\theta_i, \phi_i), Y_l^{m*}(\theta_i, \phi_i) \rangle =$$
$$\int_0^{2\pi} \int_0^{\pi} S(\theta_i, \phi_i) Y_l^{m*}(\theta_i, \phi_i) sin\theta d\theta d\phi \tag{20}$$

where $*$ denotes the complex conjugate. The estimated signal is then simply recovered by evaluating 19. The next natural question is how to transform the diffusion signal to a real spherical function, the Orientation Distribution Function (ODF), that we can use to perform fiber tractography. This reconstruction is based on the Funk-Radon transform (FRT) [25].Given a three-dimensional function $f(x)$, where x is a three-dimensional vector, the FRT at a particular radius r for a direction u is:

$$F[f(x)](u, r) = \int f(x)\delta(x^T u)\delta(|x| - r)dx \tag{21}$$

Intuitively, the FRT at a given spherical point is the great circle integral of the signal on the sphere defined by the plane through the origin equatorial to the point of evaluation. Analytically, the ODF can be obtained from the spherical harmonics estimation of HARDI signal **S** [19, 33, 1]:

$$\Psi(\theta, \phi) = \sum_{j=1}^{R} 2\pi \frac{c_j}{S_0} P_{l(j)} Y_j(\theta, \phi) \tag{22}$$

where $P_{l(j)}$ is the Legendre polynomial of order l corresponding to the jth coefficient. The reader interested in the underlying mathematics and proof for this solution is referred to [18] for all the details.

Finally, in order to improve the the angular resolution of the ODF, since they are "blurry" in nature, a new object is needed for fiber tractography purposes. This object is called fiber orientation distribution (FOD) and is computed using a spherical deconvolution [66].

The idea is that $\mathbf{S}(\theta, \phi)$ that would be measured from a sample containing several distinct fiber populations is then given by the sum of the axially symmetric response function $R(\theta)$, which is the expected diffusion properties of white matter (WM), gray matter (GM) and cerebro-spinal fluid (CSF) tissue, weighted by their respective volume fractions, and rotated such that they are aligned along their respective orientations (ϕ is the azimuthal angle in spherical coordinates):

$$\mathbf{S}(\theta, \phi) = \sum_i f_i \hat{A}_i R(\theta) \tag{23}$$

where f_i is the volume fraction for the ith fiber population, and $\hat{A}_i$ is the operator representing a rotation onto the direction (θ, ϕ). This can be expressed as the convolution over the unit sphere of the response function $R(\theta)$ with a fiber orientation density function $F(\theta, \phi)$:

$$\mathbf{S}(\theta, \phi) = F(\theta, \phi) \circledast R(\theta) \tag{24}$$

However is the $F(\theta, \phi)$ what we want to construct. To do this, it is as simple as deconvolve: $F(\theta, \phi) = \mathbf{S}(\theta, \phi) \circledast^{-1} R(\theta)$. An example of the constructed FOD for each voxel is represented in figure 6.A.
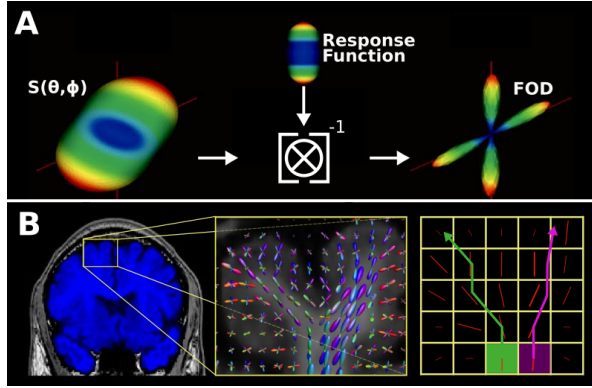

Fig. 3. A. Spherical deconvolution intuition to improve angular resolution of ODF reconstruction, modify from [17]. B. Right panel shows the volume fraction maps, mid panel the ODFs (left-right/front-back/up-down) and left the reconstructed tract starting from two different voxels panel, modify from [38]. Buscar permisos si es necesario

Now that we have the $F(\theta, \phi)$ for each voxel, we can try to reconstruct the white matter tracts. A primary assumption of many deterministic tractography algorithms is that the direction of greatest diffusivity is roughly parallel to the local white matter fiber bundle direction. The simplest tractography algorithms follow the major eigenvector direction at discrete locations in small, discrete steps. This assumption can lead to inaccuracies, especially in regions where multiple fiber populations are present, such as fiber crossings or complex branching areas.

To address these limitations, probabilistic tractography methods explicitly model uncertainty and allow for the generation of multiple pathways as probability map. Once fiber-orientation probability density functions (PDFs) have been generated for each voxel in the brain (see Estimation of Fiber Orientation PDFs for Probabilistic Tractography in [39]), it is possible to simulate the likely range of outputs of a deterministic tracking process using a multitude of approaches such as Monte Carlo techniques were within each run it is use a randomly selected sample from each PDF [60], it is also possible to invoke the diffusion process itself as a propagator for the tractography process as a random

walk [42], or attempt to identify routes through the brain by front propagation methods [7].

Whatever the probabilistic approach used, a reconstruction of the tracts similar to that in the figure 5 is generated. The current state of the art in tractography has been addressed by [30], where fourteen teams, adding up to 57 researchers, participate on a challenge to estimate the ground-truth connectivity of three numerical phantoms.
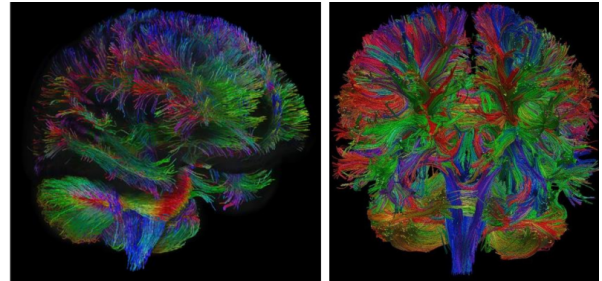

Fig. 4. Example whole-brain fibre-tracking results from human healthy subject (left-right/front-back/up-down). Buscar referencia.

Finally, the whole brain connectome was computed for the s200 atlas. The connectivity matrix $\mathcal{G} = \{\mathcal{V}, \mathcal{E}, \mathbf{A}\}$, with entries on the adjacency matrix $\mathbf{A}(i, j)$, represents the strength or number of connections between ROIs. Figure x.A shows the mean normalize connectome for the 606 subjects, which standard deviation is shown in Figure x.B.
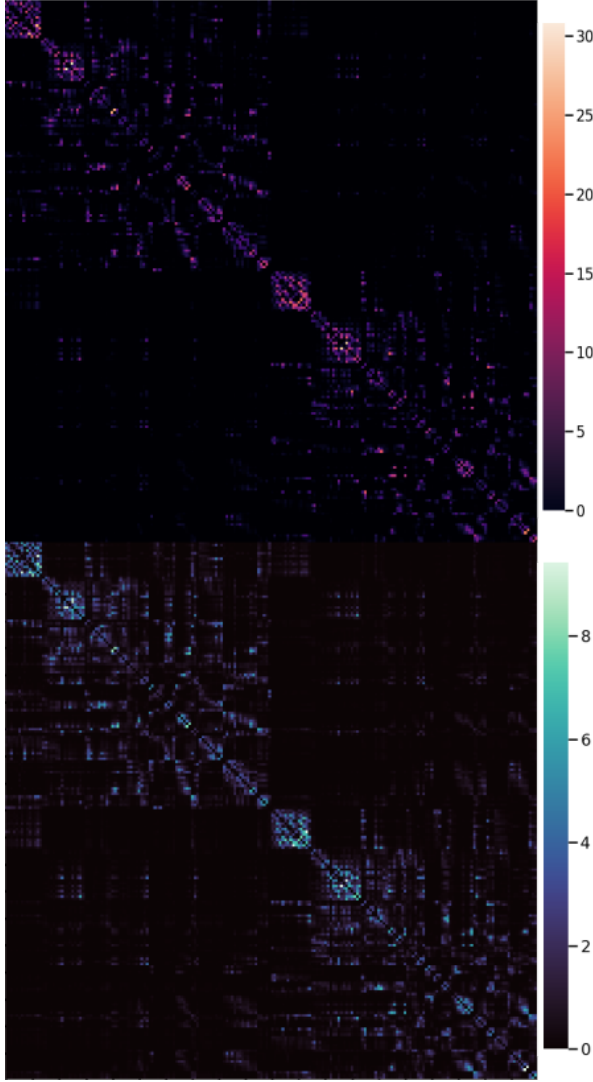
Fig. 5. Mean and Standard Deviation connectome calculated for the 606 subjects

procesamiento connectividad GCN Related work Results Citas

The estimation of tissue fiber response functions, which is the expected diffusion properties of white matter (WM), gray matter (GM) and cerebro-spinal fluid (CSF) tissue, was carried out using the dhollander algorithm, and fiber orientation distributions (FODs) were estimated using the multi-shell multi-tissue constrained spherical deconvolution (MSMT-CSD) algorithm. Probability tractography was implemented using the iFOD2 probabilistic tracking method. Anatomically-constrained tractography

(ACT) was applied, incorporating T1-weighted (T1w) segmentation constraints. The T1w segmentation utilized FreeSurfer outputs from the anatomical processing steps, enabling the hybrid surface volume segmentation (HSVS) method.

, we employed the `mrtrix_multishell_msmt_ACT-hsvs` pipeline

Streamline weights for the structural connectivity matrix were calculated using the SIFT2 algorithm, ensuring a refined representation of white matter connections. For a comprehensive understanding of the original preprocessing details executed by QSIprep, we direct readers to Supplementary X, where a detailed documentation of the preprocessing steps is available. This supplementary information serves as a valuable reference, providing transparency and reproducibility insights into the diffusion MRI preprocessing procedures applied in this study.

3.4 Graph Convolutional Network

Classic convolutional neural network (CNN) models designed for grid-like data, such as images, have demonstrated considerable success in various applications, including image classification [46,47,48], object detection [18, 49], and semantic segmentation [50, 51]. The efficacy of these models relies on inherent properties of grid-like data, specifically: (1) a fixed number of neighboring pixels for each pixel and (2) a naturally determined spatial order when scanning images, i.e., from left to right and top to bottom. However, in arbitrary graph data, unlike images, neither the number of neighboring units nor their spatial order is fixed.

In this context, our focus is on Graph Convolutional Network (GCN) models applied to undirected connected graphs $\mathcal{G} = \mathcal{V}, \mathcal{E}, \mathbf{A}$. The connectivity measurements used in our study give rise to such graphs, consisting of a set of nodes $\mathcal{V}$ with $|\mathcal{V}| = n$, a set of edges $\mathcal{E}$ with $|\mathcal{E}| = m$, and an adjacency matrix $\mathbf{A}$. If there is an edge between node i and node j, the entry $\mathbf{A}(i,j)$ denotes the weight of the edge; otherwise, $\mathbf{A}(i,j) = 0$.

$$A_k(n) = \frac{1}{L} \sum_{j=0}^{L-1} X_k(j) W(j) e^{-i\frac{2kj}{L}} \tag{25}$$

Node attributes, are represented as $\mathbf{X} \in \mathbb{R}^{n \times d}$, where d is the length of the attributes for each node n. In our case, these attributes include the concatenated
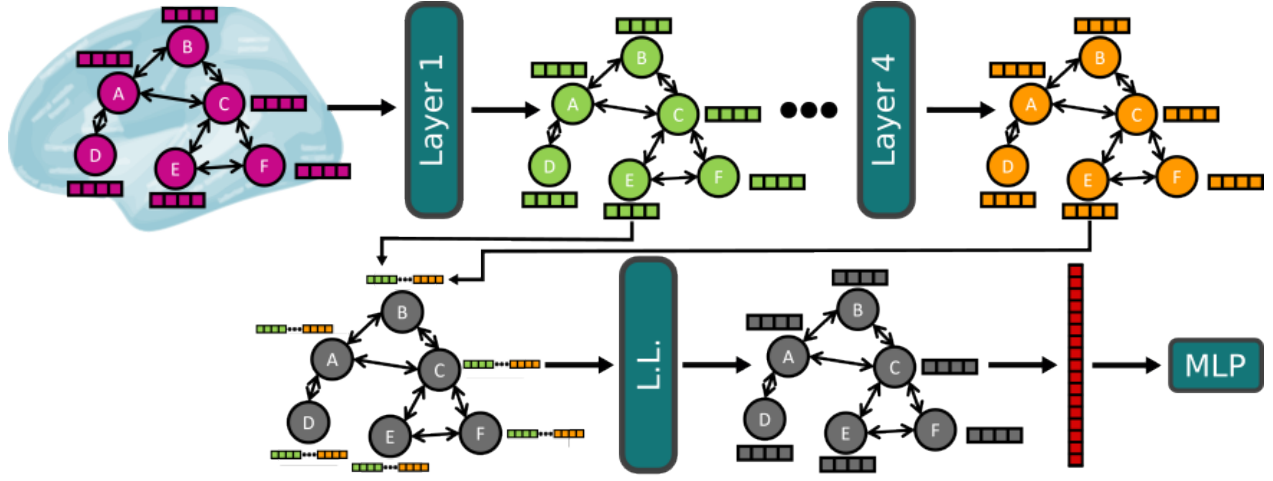
Fig. 6. A.

PCA(PSD) and morphometric features for each ROI. The multi-layer GCN used, follows the layer-wise propagation rule:

$$\mathbf{H}^{(l+1)} = \sigma \left(\hat{\mathbf{D}}^{-\frac{1}{2}} \hat{\mathbf{A}} \hat{\mathbf{D}}^{-\frac{1}{2}} \mathbf{H}^l \mathbf{W}^l \right). \qquad (26)$$

Here, $\hat{\mathbf{A}} = \mathbf{A} + \mathbf{I}_N$, equivalent to adding self-loops to the original graph. $\mathbf{I}_N$ is the identity matrix, $\hat{\mathbf{D}}ii = \sum_j \hat{\mathbf{A}}ij$ is used for neighborhood normalization, and W^l is a layer-specific trainable weight matrix. $\sigma(\cdot)$ denotes an activation function, such as $ReLU(\cdot) = \max(0, \cdot)$. $\mathbf{H}^l \in \mathbb{R}^{n \times d}$ is the matrix of activations in the lth layer, with $\mathbf{H}^0 = \mathbf{X}$.

This layer-wise approach implies that in each layer, a node u updates its attributes by aggregating information only from nodes $\{\forall v \in \mathcal{N}\{u\}\}$. The addition of more layers allows the aggregation of more distant neighbors. The output of the final layer can then be used to define the embeddings for each node, i.e.,

$$\mathbf{z}_u = h_u^k, \forall u \in \mathcal{V} \qquad (27)$$

where k represent the last layer. However, caution is warranted as a very deep network may oversample the graph and, in the worst case, cover the entire graph.

Let's recall that the graphs in question represent individualized connectomes, and our objective is to forecast a property related to the entire graph - specifically, the biological age of the subjects. In contrast to learning a node-level embedding $\mathbf{z}u$, our aim is to acquire a graph-level embedding $\mathbf{z_G}$. This undertaking is commonly termed "graph pooling," as it involves aggregating node embeddings to derive an embedding that encapsulates the entire graph.

The pooling function f_p, which has to be ordering and permutation invariant, maps a set of node embeddings $\{\mathbf{z}_1, \ldots, \mathbf{z}_{|V|}\}$ to an embedding $\mathbf{z_G}$. Here a global mean pooling approach was taken, where:

$$\mathbf{z_G} = \frac{\sum_{i=0}^{|\mathcal{V}|} \mathbf{z}_u}{|\mathcal{V}|} \qquad (28)$$
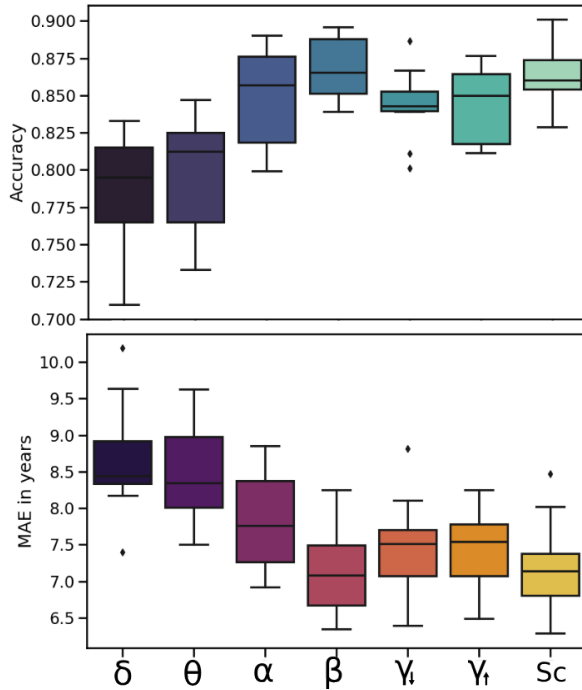
4 Results

Fig. 7. caption

5 Conclusion and Future Work

Conclusions here.

Acknowledgements

References

1. **Anderson, A. W. (2005).** Measurement of fiber orientation distributions using high angular resolution diffusion imaging. *Magnetic Resonance in Medicine: An Official Journal of the International Society for Magnetic Resonance in Medicine*, Vol. 54, No. 5, pp. 1194–1206.

2. **Baecker, L., Garcia-Dias, R., Vieira, S., Scarpazza, C., & Mechelli, A. (2021).** Machine learning for brain age prediction: Introduction to methods and clinical applications. *EBioMedicine*, Vol. 72.

3. **Basser, P. J., Mattiello, J., & LeBihan, D. (1994).** Estimation of the effective self-diffusion tensor from the nmr spin echo. *Journal of Magnetic Resonance, Series B*, Vol. 103, No. 3, pp. 247–254.

4. **Bi, S., Guan, Y., & Tian, L. (2024).** Prediction of individual brain age using movie and resting-state fmri. *Cerebral Cortex*, Vol. 34, No. 1, pp. bhad407.

5. **Borkar, K., Chaturvedi, A., Vinod, P., & Bapi, R. S. (2022).** Ayu-characterization of healthy aging from neuroimaging data with deep learning and rsfmri. *Frontiers in Computational Neuroscience*, Vol. 16, pp. 940922.

6. **Bruns, A., Eckhorn, R., Jokeit, H., & Ebner, A. (2000).** Amplitude envelope correlation detects coupling among incoherent brain signals. *Neuroreport*, Vol. 11, No. 7, pp. 1509–1514.

7. **Campbell, J. S., Siddiqi, K., Rymar, V. V., Sadikot, A. F., & Pike, G. B. (2005).** Flow-based fiber tracking with diffusion tensor and q-ball data: validation and comparison to principal diffusion direction techniques. *NeuroImage*, Vol. 27, No. 4, pp. 725–736.

8. **Chen, C.-L., Hsu, Y.-C., Yang, L.-Y., Tung, Y.-H., Luo, W.-B., Liu, C.-M., Hwang, T.-J., Hwu, H.-G., & Tseng, W.-Y. I. (2020).** Generalization of diffusion magnetic resonance imaging–based brain age prediction model through transfer learning. *NeuroImage*, Vol. 217, pp. 116831.

9. **Cohen, M. X. (2014).** *Analyzing neural time series data: theory and practice*. MIT press.

10. **Cole, J. H., Annus, T., Wilson, L. R., Remtulla, R., Hong, Y. T., Fryer, T. D., Acosta-Cabronero, J., Cardenas-Blanco, A., Smith, R., Menon, D. K., et al. (2017).** Brain-predicted age in down syndrome is associated with beta amyloid deposition and cognitive decline. *Neurobiology of aging*, Vol. 56, pp. 41–49.

11. **Cole, J. H., Leech, R., Sharp, D. J., & Initiative, A. D. N. (2015).** Prediction of brain age suggests accelerated atrophy after traumatic brain injury. *Annals of neurology*, Vol. 77, No. 4, pp. 571–581.

12. **Cole, J. H., Underwood, J., Caan, M. W., De Francesco, D., Van Zoest, R. A., Leech, R., Wit, F. W., Portegies, P., Geurtsen, G. J., Schmand, B. A., et al. (2017).** Increased brain-predicted aging in treated hiv disease. *Neurology*, Vol. 88, No. 14, pp. 1349–1357.

13. **da Silva Castanheira, J., Orozco Perez, H. D., Misic, B., & Baillet, S. (2021).** Brief segments

of neurophysiological activity enable individual differentiation. *Nature communications*, Vol. 12, No. 1, pp. 5713.

14. **Dale, A. M., Fischl, B., & Sereno, M. I. (1999).** Cortical surface-based analysis: I. segmentation and surface reconstruction. *Neuroimage*, Vol. 9, No. 2, pp. 179–194.

15. **Damoiseaux, J. S. (2017).** Effects of aging on functional and structural brain connectivity. *Neuroimage*, Vol. 160, pp. 32–40.

16. **de Lange, A.-M. G., Anatürk, M., Rokicki, J., Han, L. K., Franke, K., Alnæs, D., Ebmeier, K. P., Draganski, B., Kaufmann, T., Westlye, L. T., et al. (2022).** Mind the gap: Performance metric evaluation in brain-age prediction. *Human Brain Mapping*, Vol. 43, No. 10, pp. 3113–3129.

17. **Descoteaux, M. (1999).** High angular resolution diffusion imaging (hardi). *Wiley encyclopedia of electrical and electronics engineering*, pp. 1–25.

18. **Descoteaux, M. (2008).** *High angular resolution diffusion MRI: from local estimation to segmentation and tractography*. Ph.D. thesis, Université Nice Sophia Antipolis.

19. **Descoteaux, M., Angelino, E., Fitzgibbons, S., & Deriche, R. (2007).** Regularized, fast, and robust analytical q-ball imaging. *Magnetic Resonance in Medicine: An Official Journal of the International Society for Magnetic Resonance in Medicine*, Vol. 58, No. 3, pp. 497–510.

20. **Dinsdale, N. K., Bluemke, E., Smith, S. M., Arya, Z., Vidaurre, D., Jenkinson, M., & Namburete, A. I. (2021).** Learning patterns of the ageing brain in mri using deep convolutional networks. *NeuroImage*, Vol. 224, pp. 117401.

21. **Engemann, D. A., Mellot, A., Höchenberger, R., Banville, H., Sabbagh, D., Gemein, L., Ball, T., & Gramfort, A. (2022).** A reusable benchmark of brain-age prediction from m/eeg resting-state signals. *Neuroimage*, Vol. 262, pp. 119521.

22. **Feng, X., Lipton, Z. C., Yang, J., Small, S. A., Provenzano, F. A., Initiative, A. D. N., Initiative, F. L. D. N., et al. (2020).** Estimating brain age based on a uniform healthy population with deep learning and structural magnetic resonance imaging. *Neurobiology of aging*, Vol. 91, pp. 15–25.

23. **Fingelkurts, A. A., Fingelkurts, A. A., & Kähkönen, S. (2005).** Functional connectivity in the brain—is it an elusive concept? *Neuroscience & Biobehavioral Reviews*, Vol. 28, No. 8, pp. 827–836.

24. **Franke, K. & Gaser, C. (2012).** Longitudinal changes in individual brainage in healthy aging, mild cognitive impairment, and alzheimer's disease. *GeroPsych*.

25. **Funk, P. (1915).** Uber eine geometrische anwendung der abelschen integralgleichung. *Mathematische Annalen*, Vol. 77, No. 1, pp. 129–135.

26. **Gao, X. & Pang, Y. (2022).** Brain age prediction with 3d resnet34 model in healthy control, mild cognitive impairment, and alzheimer's disease. *2022 3rd International Conference on Electronic Communication and Artificial Intelligence (IWECAI)*, IEEE, pp. 490–494.

27. **Gaser, C., Franke, K., Klöppel, S., Koutsouleris, N., Sauer, H., & Initiative, A. D. N. (2013).** Brainage in mild cognitive impaired patients: predicting the conversion to alzheimer's disease. *PloS one*, Vol. 8, No. 6, pp. e67346.

28. **Gemein, L. A., Schirrmeister, R. T., Boedecker, J., & Ball, T. (2023).** Brain age revisited: Investigating the state vs. trait hypotheses of eeg-derived brain-age dynamics with deep learning. *arXiv preprint arXiv:2310.07029*.

29. **Gianchandani, N., Ospel, J., MacDonald, E., & Souza, R. (2023).** A multitask deep learning model for voxel-level brain age estimation. *International Workshop on Machine Learning in Medical Imaging*, Springer, pp. 283–292.

30. **Girard, G., Rafael-Patiño, J., Truffet, R., Aydogan, D. B., Adluru, N., Nair, V. A., Prabhakaran, V., Bendlin, B. B., Alexander, A. L., Bosticardo, S., et al. (2023).** Tractography passes the test: Results from the diffusion-simulated connectivity (disco) challenge. *NeuroImage*, Vol. 277, pp. 120231.

31. **Gonneaud, J., Baria, A. T., Binette, A. P., Gordon, B. A., Chhatwal, J. P., Cruchaga, C., Jucker, M., Levin, J., Salloway, S., Farlow, M., et al. (2020).** Functional brain age prediction suggests accelerated aging in preclinical familial alzheimer's disease, irrespective of fibrillar amyloid-beta pathology. *bioRxiv*, pp. 2020–05.

32. **Gross, J., Baillet, S., Barnes, G. R., Henson, R. N., Hillebrand, A., Jensen, O., Jerbi, K., Litvak, V., Maess, B., Oostenveld, R., et al. (2013).** Good practice for conducting and reporting meg research. *Neuroimage*, Vol. 65, pp. 349–363.

33. **Hess, C. P., Mukherjee, P., Han, E. T., Xu, D., & Vigneron, D. B. (2006).** Q-ball reconstruction of multimodal fiber orientations using the spherical

harmonic basis. *Magnetic Resonance in Medicine: An Official Journal of the International Society for Magnetic Resonance in Medicine*, Vol. 56, No. 1, pp. 104–117.

34. **Hipp, J. F., Hawellek, D. J., Corbetta, M., Siegel, M., & Engel, A. K. (2012).** Large-scale cortical correlation structure of spontaneous oscillatory activity. *Nature neuroscience*, Vol. 15, No. 6, pp. 884–890.

35. **Holler, V. M., .** "from signal to age-using machine learning to predict brain age from meg data" masterarbeit.

36. **Huang, M., Mosher, J. C., & Leahy, R. (1999).** A sensor-weighted overlapping-sphere head model and exhaustive head model comparison for meg. *Physics in Medicine & Biology*, Vol. 44, No. 2, pp. 423.

37. **Isaev, N. K., Genrikhs, E. E., Oborina, M. V., & Stelmashook, E. V. (2018).** Accelerated aging and aging process in the brain. *Reviews in the Neurosciences*, Vol. 29, No. 3, pp. 233–240.

38. **Jeurissen, B., Tournier, J.-D., Dhollander, T., Connelly, A., & Sijbers, J. (2014).** Multi-tissue constrained spherical deconvolution for improved analysis of multi-shell diffusion mri data. *NeuroImage*, Vol. 103, pp. 411–426.

39. **Jones, D. K. (2010).** *Diffusion mri*. Oxford University Press.

40. **Jones, D. K., Horsfield, M. A., & Simmons, A. (1999).** Optimal strategies for measuring diffusion in anisotropic systems by magnetic resonance imaging. *Magnetic Resonance in Medicine: An Official Journal of the International Society for Magnetic Resonance in Medicine*, Vol. 42, No. 3, pp. 515–525.

41. **Joo, Y., Namgung, E., Jeong, H., Kang, I., Kim, J., Oh, S., Lyoo, I. K., Yoon, S., & Hwang, J. (2023).** Brain age prediction using combined deep convolutional neural network and multi-layer perceptron algorithms. *Scientific Reports*, Vol. 13, No. 1, pp. 22388.

42. **Koch, M. A., Norris, D. G., & Hund-Georgiadis, M. (2002).** An investigation of functional and anatomical connectivity using magnetic resonance imaging. *Neuroimage*, Vol. 16, No. 1, pp. 241–250.

43. **Koutsouleris, N., Davatzikos, C., Borgwardt, S., Gaser, C., Bottlender, R., Frodl, T., Falkai, P., Riecher-Rössler, A., Möller, H.-J., Reiser, M., et al. (2014).** Accelerated brain aging in schizophrenia and beyond: a neuroanatomical marker of psychiatric disorders. *Schizophrenia bulletin*, Vol. 40, No. 5, pp. 1140–1153.

44. **Kruskal, J. B. (1956).** On the shortest spanning subtree of a graph and the traveling salesman problem. *Proceedings of the American Mathematical society*, Vol. 7, No. 1, pp. 48–50.

45. **Kuhn, T., Kaufmann, T., Doan, N. T., Westlye, L. T., Jones, J., Nunez, R. A., Bookheimer, S. Y., Singer, E. J., Hinkin, C. H., & Thames, A. D. (2018).** An augmented aging process in brain white matter in hiv. *Human brain mapping*, Vol. 39, No. 6, pp. 2532–2540.

46. **Lancaster, J., Lorenz, R., Leech, R., & Cole, J. H. (2018).** Bayesian optimization for neuroimaging pre-processing in brain age classification and prediction. *Frontiers in aging neuroscience*, Vol. 10, pp. 28.

47. **Lee, W. H. (2023).** The choice of machine learning algorithms impacts the association between brain-predicted age difference and cognitive function. *Mathematics*, Vol. 11, No. 5, pp. 1229.

48. **Li, H., Satterthwaite, T. D., & Fan, Y. (2018).** Brain age prediction based on resting-state functional connectivity patterns using convolutional neural networks. *2018 ieee 15th international symposium on biomedical imaging (isbi 2018)*, IEEE, pp. 101–104.

49. **Li, Y., Zhang, X., Nie, J., Zhang, G., Fang, R., Xu, X., Wu, Z., Hu, D., Wang, L., Zhang, H., et al. (2022).** Brain connectivity based graph convolutional networks and its application to infant age prediction. *IEEE Transactions on Medical Imaging*, Vol. 41, No. 10, pp. 2764–2776.

50. **Lin, L., Jin, C., Fu, Z., Zhang, B., Bin, G., & Wu, S. (2016).** Predicting healthy older adult's brain age based on structural connectivity networks using artificial neural networks. *Computer methods and programs in biomedicine*, Vol. 125, pp. 8–17.

51. **Luders, E., Cherbuin, N., & Gaser, C. (2016).** Estimating brain age using high-resolution pattern recognition: Younger brains in long-term meditation practitioners. *Neuroimage*, Vol. 134, pp. 508–513.

52. **Maier-Hein, K. H., Neher, P. F., Houde, J.-C., Côté, M.-A., Garyfallidis, E., Zhong, J., Chamberland, M., Yeh, F.-C., Lin, Y.-C., Ji, Q., et al. (2017).** The challenge of mapping the human connectome based on diffusion tractography. *Nature communications*, Vol. 8, No. 1, pp. 1349.

53. **Massett, R. J., Maher, A. S., Imms, P. E., Amgalan, A., Chaudhari, N. N., Chowdhury, N. F.,**

Irimia, A., & Initiative, A. D. N. (2023). Regional neuroanatomic effects on brain age inferred using magnetic resonance imaging and ridge regression. *The Journals of Gerontology: Series A*, Vol. 78, No. 6, pp. 872–881.

54. Monti, R. P., Gibberd, A., Roy, S., Nunes, M., Lorenz, R., Leech, R., Ogawa, T., Kawanabe, M., & Hyvärinen, A. (2020). Interpretable brain age prediction using linear latent variable models of functional connectivity. *Plos one*, Vol. 15, No. 6, pp. e0232296.

55. More, S., Antonopoulos, G., Hoffstaedter, F., Caspers, J., Eickhoff, S. B., Patil, K. R., Initiative, A. D. N., et al. (2023). Brain-age prediction: A systematic comparison of machine learning workflows. *NeuroImage*, Vol. 270, pp. 119947.

56. Nguyen, H.-D., Clément, M., Mansencal, B., & Coupé, P. (2024). Brain structure ages—a new biomarker for multi-disease classification. *Human Brain Mapping*, Vol. 45, No. 1, pp. e26558.

57. Nikiforov, A. F. & Uvarov, B., Vasili (1988). *Special functions of mathematical physics*, volume 205. Springer.

58. Onaolapo, A. Y., Obelawo, A. Y., & Onaolapo, O. J. (2019). Brain ageing, cognition and diet: a review of the emerging roles of food-based nootropics in mitigating age-related memory decline. *Current aging science*, Vol. 12, No. 1, pp. 2–14.

59. Pardoe, H. R., Cole, J. H., Blackmon, K., Thesen, T., Kuzniecky, R., Investigators, H. E. P., et al. (2017). Structural brain changes in medically refractory focal epilepsy resemble premature brain aging. *Epilepsy research*, Vol. 133, pp. 28–32.

60. Parker, G. J. & Alexander, D. C. (2005). Probabilistic anatomical connectivity derived from the microscopic persistent angular structure of cerebral tissue. *Philosophical transactions of the Royal Society B: Biological sciences*, Vol. 360, No. 1457, pp. 893–902.

61. Sala-Llonch, R., Bartrés-Faz, D., & Junqué, C. (2015). Reorganization of brain networks in aging: a review of functional connectivity studies. *Frontiers in psychology*, Vol. 6, pp. 136321.

62. Shafto, M. A., Tyler, L. K., Dixon, M., Taylor, J. R., Rowe, J. B., Cusack, R., Calder, A. J., Marslen-Wilson, W. D., Duncan, J., Dalgleish, T., et al. (2014). The cambridge centre for ageing and neuroscience (cam-can) study protocol: a cross-sectional, lifespan, multidisciplinary examination of healthy cognitive ageing. *BMC neurology*, Vol. 14, pp. 1–25.

63. Steffener, J., Habeck, C., O'Shea, D., Razlighi, Q., Bherer, L., & Stern, Y. (2016). Differences between chronological and brain age are related to education and self-reported physical activity. *Neurobiology of aging*, Vol. 40, pp. 138–144.

64. Tadel, F., Baillet, S., Mosher, J. C., Pantazis, D., & Leahy, R. M. (2011). Brainstorm: a user-friendly application for meg/eeg analysis. *Computational intelligence and neuroscience*, Vol. 2011, pp. 1–13.

65. Taylor, J. R., Williams, N., Cusack, R., Auer, T., Shafto, M. A., Dixon, M., Tyler, L. K., Henson, R. N., et al. (2017). The cambridge centre for ageing and neuroscience (cam-can) data repository: Structural and functional mri, meg, and cognitive data from a cross-sectional adult lifespan sample. *neuroimage*, Vol. 144, pp. 262–269.

66. Tournier, J.-D., Calamante, F., Gadian, D. G., & Connelly, A. (2004). Direct estimation of the fiber orientation density function from diffusion-weighted mri data using spherical deconvolution. *Neuroimage*, Vol. 23, No. 3, pp. 1176–1185.

67. Uusitalo, M. A. & Ilmoniemi, R. J. (1997). Signal-space projection method for separating meg or eeg into components. *Medical and biological engineering and computing*, Vol. 35, pp. 135–140.

68. Vecchio, L. M., Meng, Y., Xhima, K., Lipsman, N., Hamani, C., & Aubert, I. (2018). The neuroprotective effects of exercise: maintaining a healthy brain throughout aging. *Brain plasticity*, Vol. 4, No. 1, pp. 17–52.

69. Wold, S., Esbensen, K., & Geladi, P. (1987). Principal component analysis. *Chemometrics and intelligent laboratory systems*, Vol. 2, No. 1-3, pp. 37–52.

70. Xu, L., Ma, H., Guan, Y., Liu, J., Huang, H., Zhang, Y., & Tian, L. (2023). A siamese network with node convolution for individualized predictions based on connectivity maps extracted from resting-state fmri data. *IEEE Journal of Biomedical and Health Informatics*.

71. Yankner, B. A., Lu, T., & Loerch, P. (2008). The aging brain. *Annu. Rev. Pathol. Mech. Dis.*, Vol. 3, pp. 41–66.

72. Yeo, B. T., Krienen, F. M., Sepulcre, J., Sabuncu, M. R., Lashkari, D., Hollinshead, M., Roffman, J. L., Smoller, J. W., Zöllei, L., Polimeni, J. R., et al. (2011). The organization of the human

cerebral cortex estimated by intrinsic functional connectivity. *Journal of neurophysiology*.

73. **Zeighami, Y. & Evans, A. C. (2021).** Association vs. prediction: the impact of cortical surface smoothing and parcellation on brain age. *Frontiers in big Data*, Vol. 4, pp. 637724.

74. **Zhang, J. & Liu, C. (2015).** On linearly constrained minimum variance beamforming. *The Journal of Machine Learning Research*, Vol. 16, No. 1, pp. 2099–2145.

75. **Zhuang, P., Toro, C., Grafman, J., Manganotti, P., Leocani, L., & Hallett, M. (1997).** Event-related desynchronization (erd) in the alpha frequency during development of implicit and explicit learning. *Electroencephalography and clinical neurophysiology*, Vol. 102, No. 4, pp. 374–381.